replaced by open stubs. The design methodology is nearly the same with the previous one. The dimensions are determined as follows: $L_{17} = 9.8$ mm, $L_{18} = 11.6$ mm, $L_{19} = 3.9$ mm, $L_{20} = 5.8$ mm, $L_{21} = 5.9$ mm, $L_{22} = 3$ mm, $L_{23} = 18.7$ mm, $L_{24} = 1.9$ mm, $L_{25} = 3.6$ mm, $L_{26} = 2$ mm, $W_7 = 0.92$ mm, $W_8 = 0.8$ mm, $W_9 = 1.6$ mm, $W_{10} = 1.6$ mm, $W_{11} = 1$ mm, $g_6 = 0.2$ mm, $g_7 = 1.6$ mm, $g_8 = 1$ mm. The photograph of the fabricated dual-band filter is shown in Figure 8.

Figure 9 shows the simulated and measured results of the filter. Good agreement between them is observed. One passband is centered at 2.44 GHz, has the 3 dB bandwidth of 13.9%. The minimum insertion loss is measured to be 1.1 dB. The return loss within the passband is greater than 23 dB. The other passband is located at 5.20 GHz with the 3 dB bandwidth of 8.3%. The measured insertion loss is 1.8 dB and the return loss is greater than 16 dB. Four transmission zeros are realized at 1.46, 2.89, 4.6, and 5.7 GHz.

5. CONCLUSION

Two high-selectivity dual-band bandpass filters has been presented. The resonant frequencies can be individually controlled. Using short and open stubs as loading elements, dual-band BPFs can be designed with flexibly controlled passband frequency ranges. Four transmission zeros are realized near the passband edges, resulting in high selectivity. The simple planar structure as well as high selectivity makes them attractive for many applications.

ACKNOWLEDGMENT

This project is supported by NSFC under 61001055 and U1035002, the Shenzhen Science and Technology Planning Project under JC201005280584A and by the Shenzhen Science and Technology Planning Project for the Establishment of Key Laboratory in 2009 (CXB200903090021A).

REFERENCES

1. M. Sagawa, M. Makimoto, and S. Yamashita, Geometrical structures and fundamental characteristics of microwave stepped-impedance resonators, IEEE Trans Microwave Theory Tech 45 (1997), 1078–1085.
2. C.-W. Tang and P.-H. Wu, Design of a planar dual-band bandpass filter, IEEE Microwave Wireless Compon Lett 21 (2011), 362–364.
3. L. Guo, Z.-Y. Yu, and L. Zhang, A dual-band band-pass filter using stepped impedance resonator, Microwave Opt Technol Lett 53 (2011), 123–125.
4. X.Y. Zhang, J. Shi, J.-X. Chen, and Q. Xue, Dual-band bandpass filter design using a novel feed scheme, IEEE Microwave Wireless Compon Lett 19 (2009), 350–352.
5. G.L. Dai, Y.X. Guo, and M.Y. Xia, Dual-band bandpass filter using parallel short-ended feed scheme, IEEE Microwave Wireless Compon Lett 20 (2010), 350–352.
6. J.P. Wang, J. Ni, J.-B. Pan, L. Ge, and Y.-X. Guo, Design of miniaturized microstrip dual-mode dual-band bandpass filter, Microwave Opt Technol Lett 53 (2011), 1493–1496.
7. X.Y. Zhang, J.-X. Chen, Q. Xue, and S.-M. Li, Dual-band bandpass filter using stub-loaded resonators, IEEE Microwave Wireless Compon Lett 17 (2007), 583–585.
8. F.-C. Cheng, Q.-X. Chu, and Z.-H. Tu, Design of compact dual-band bandpass filter using short stub loaded resonator, Microwave Opt Technol Lett 51 (2009), 959–963.
9. W.Q. He, Z.W. Ma, C.-P. Chen, T. Anada, and Y. Kobayashi, A compact dual-band bandpass filter using stub-loaded two mode resonators and direct source-load coupling to obtain improved stopband characteristics, Microwave Opt Technol Lett 51 (2009), 618–621.

DESIGN OF GRADED INDEX FLAT LENSES WITH INTEGRATED ANTIREFLECTIVE PROPERTIES

Brandon Good,[1] Paul Ransom,[1] Shaun Simmons,[1] Austin Good,[2] and Mark S. Mirotznik[2]

[1] Naval Surface Warfare Center, Carderock MD, 9500 Macarthur Blvd., Carderock, MD 22314

[2] Department of Electrical and Computer Engineering, The University of Delaware, Newark, DE 19716; Corresponding author: mirotzni@udel.edu

Received 23 March 2012

ABSTRACT: *We describe a new methodology for designing graded index lenses at microwave wavelengths with integrated antireflective properties. The method leads to a flat lens with minimal reflection losses at a frequency of interest. Both numerical and experimental results for two different design goals are shown to demonstrate the capabilities of the methodology.* © 2012 Wiley Periodicals, Inc. Microwave Opt Technol Lett 54:2774–2781, 2012; View this article online at wileyonlinelibrary.com. DOI 10.1002/mop.27198

Key words: *flat lens; graded index lens; antireflective; subwavelength; rigorous coupled-wave*

1. INTRODUCTION

In this article, we describe a new design method for realizing various graded index lenses (GRIN) with integrated antireflective (AR) properties. Our method uses an aperiodic subwavelength surface structure creating an ''effective'' index of refraction that varies spatially and, thus, can be used to realize GRIN lenses or other GRIN-based optical elements. Other authors have demonstrated how aperiodic subwavelength surfaces can be used to create a spatial variation of effective dielectric properties (i.e., GRIN) [1–6]. This previous work was useful for creating flat optical elements, such as lenses, however, it did not account for loss in transmission due to front and back face reflections. In many cases, reflected losses can be greater than 50% when the element is fabricated from a high dielectric constant substrate. However, to realize thin GRIN elements it is advantageous to use high dielectric constant substrates. In this work, we show that by exploiting an additional degree of freedom within the subwavelength surface structure it is possible to achieve a desired GRIN profile while simultaneously accomplishing index matching in a single integrated design. This can be used to realize thin GRIN elements within high dielectric constant substrates while minimizing reflected losses. It should be noted that while the primary interest of this study was creating GRIN lenses, our technique can be applied to nearly any arbitrary subwavelength diffractive optical element in which integrated AR properties are desired.

The outline of this article is as follows. In Section 2, we describe the general design methodology to achieve a flat lens with integrated AR properties. In Section 3, we describe the experimental examples and numerical models that were used to validate our design methodology. In Section 3, we also compare the expected results with predictions from a rigorous computational model and experimental measurements.

2. DESIGN METHODOLOGY

The principal goal of our approach is to create a mapping between a desired transmitted phase distribution and a subwavelength surface structure while simultaneously minimizing

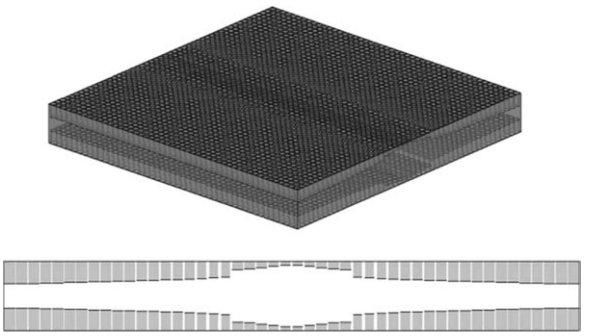

Figure 1 Conceptualize drawing of a flat lens with integrated AR properties. A subwavelength surface structure is realized by drilling electrically small cylinders into a dielectric substrate at different depths and radii. Spatial variation of both the hole depths and radii are used to create a flat lens with integrated AR properties

reflected losses (Fig. 1). To understand how this might be possible, it is useful to first describe how AR surfaces can be created using subwavelength texturing.

2.1. Subwavelength AR Surfaces

It is well-known that high quality AR surfaces can be created by fabricating single or multilevel subwavelength gratings directly on the surface of a dielectric [7–10]. This approach, originally developed for designing AR surfaces for visible and infrared applications, was biologically inspired by the subwavelength surface pattern on the cornea of many common insects including moths and many butterflies. In fact, these insect's eyes appear almost completely black due to the AR properties of its subwavelength structure. Consequently, man-made AR surfaces of this type are often called ''motheye'' surfaces. Recently, it was reported in Ref. 6 how broadband AR surfaces at microwave frequencies can be designed by drilling subwavelength cylindrical holes into a nonabsorptive dielectric substrate, shown in Figure 2. The surface structure was designed using a rigorous EM model and an iterative optimization algorithm. It was noted in Ref. 6 that an exact surface geometry to achieve good AR performance was not unique. More specifically, it is possible to find multiple geometries (i.e., different hole depths, radii, and periodicities) that achieved comparable AR performance. These different designs, while comparable from an AR perspective, did however require different amounts of dielectric material to be removed and, as a consequence, the transmitted phase through these different structures, or effective index, varied. In particular, for any given hole depth, it is possible to find a hole diameter and periodicity that has good AR properties at some given spectral frequency. It is this observation that is at the heart of the design methodology described here. By combining spatially different subwavelength grating structures—all of which achieve low reflection losses but have variable transmitted phases—it is possible to create an integrated optical element with a prescribed transmitted phase distribution but low reflection losses. In the next section, we describe this process in more detail.

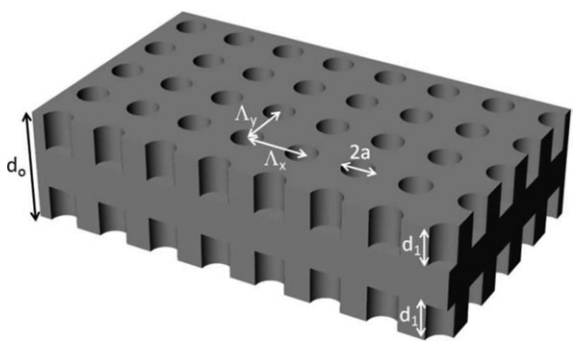

Figure 2 Geometry of structure used to calculate minimum reflection coefficient. The radius (a) of the periodic structure optimized for a given depth (d_1) and material properties ($\varepsilon_{substrate}$, μ_o)

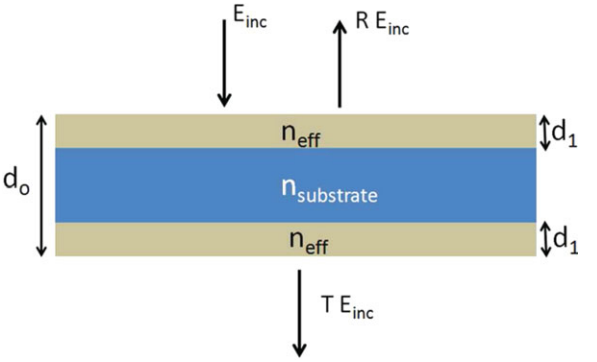

Figure 3 Infinite slab substrate of index $n_{substrate}$ is sandwiched between two identical slabs of effective index n_{eff} and thickness d_1. For these calculation, the total thickness d_o is held constant while the n_{eff} and thickness d_1 is varied. [Color figure can be viewed in the online issue, which is available at wileyonlinelibrary.com]

2.2. Mapping of Effective Index to Reflection and Phase Transmission

To understand the mapping between effective index variation, reflected energy, and transmitted phase, we first consider the simple geometry shown in Figure 3. Here, we have a dielectric slab with an index of refraction denoted by $n_{substrate}$ sandwiched between two identical dielectric slabs whose index of refraction is denoted by n_{eff} and thickness d_1. Both the incident and exit regions are assumed to be free-space. The total thickness of the sandwiched structure is denoted by d_o. We assume a normally incident plane wave of free-space wavelength λ impinges upon the structure from the top. It is well known that if the outer two slabs are formed from a material whose index of refraction is equal to $n_{eff} = \sqrt{n_{substrate}}$ and thickness, d_1, equal to a quarter wavelength (i.e., $d_1 = \frac{\lambda}{4n_{eff}}$), then the structure will be perfectly impedance matched at that frequency (e.g., zero reflected losses). However, there are many other solutions in which the structure is not perfectly matched but still has a very low reflection coefficient. This is illustrated in Figure 4. In Figure 4, we calculated the amplitude of the reflected wave and the phase of the transmitted wave as a function of the outer slabs index, n_{eff}, and thicknesses d_1.

The calculations illustrate a complicated, yet interesting, character to the reflected amplitude as one changes both the thickness and index of refraction of the outer matching layers. By inspection, there are clearly numerous solutions shown in Figure 4 in which the reflected amplitude is relatively small (<0.1) yet the transmitted phase varies considerably. In fact, it is possible to determine geometries (e.g., d_1 and n_{eff}) that have both a low reflection coefficient and a desired transmitted phase varying from 0° to over 360° while keeping the overall thickness of the structure, d_o, constant. These points are denoted by the white circles in Figure 4. It should be noted that a given solution will only be valid for a fixed wavelength, resulting in a relatively narrow band approach. It should also be noted that

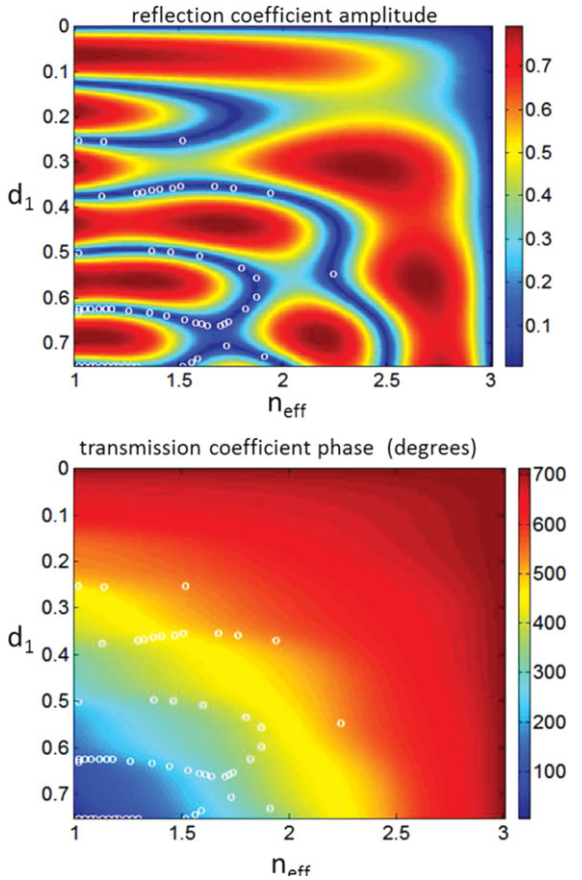

Figure 4 Calculated false color images of the reflected field amplitude (top image) and transmitted field phase (bottom image) as a function of the index of refraction, n_{eff}, and thickness, d_1, of the outer dielectric slabs shown in Figure 3. For these calculation $\lambda = 1.0$, $d_o = 1.0$, and $n_{\text{substrate}} = 3.0$. The white circles denote points in which the reflected energy is low (<5%) yet the transmitted phase angle varies over a full 360° range. [Color figure can be viewed in the online issue, which is available at wileyonlinelibrary.com]

obtaining materials with the required index of refraction is very difficult. In the next section, we discuss how to realize a particular solution using conventional materials by exploited the ''effective'' dielectric properties of subwavelength gratings.

2.3. Effective Index of Refraction via Subwavelength Gratings

To achieve a desired effective index, we employed the subwavelength grating structure depicted in Figure 2. The gratings were single level subwavelength holes with circular cross sections. This surface can be formed by drilling holes in a nonabsorptive dielectric of permittivity, $\varepsilon_{\text{substrate}}$, and index of refraction, $n_{\text{substrate}}$. To avoid any propagating diffracted orders, other than the zeroth order, the period of the gratings along the x- and y-axes, denoted by Λ_x and Λ_y respectively, should be smaller than the material wavelength. The hole radius and depth of each layer, denoted by a and d_1 respectively, were assumed variable and chosen to produce a target effective index for a specific hole depth. To calculate the grating's effective properties, we used the rigorous coupled wave (RCW) algorithm. RCW is a full wave solution that offers a balance between accuracy and computational speed. The RCW code used in this study was modeled [11–13] after the method described by Noponen and Turunen.

In Figure 5, we illustrate how the subwavelength grating structure can be used to create similar properties of antireflection and variable transmission phase shown in Figure 4. For this example, the parameters were kept the same as in Figure 4. Namely, we selected a substrate of total thickness $d_o = 1.0$, index of refraction $n_{\text{eff}} = 3.0$ and incident free-space wavelength $\lambda = 1.0$. The only difference is that instead of varying the effective index, n_{eff}, as in Figure 4, we varied the geometrical fill factor defined as the ratio of the hole diameter to grating period (i.e., fill factor $= 2a/\Lambda$). The period for this case was assumed the same along both the x and y axes (i.e., $\Lambda_x = \Lambda_y = \Lambda$) and fixed to a value of 1/10th the free-space wavelength. This periodicity is small enough to ensure only the zeroth diffractive order propagates. We used RCW to calculate reflection and transmission coefficients for illumination by a normally incident plane wave. The top image presents a false color image of the RCW calculated reflection coefficient (magnitude) as a function of both hole depth and fill factor. The bottom image presents the transmitted phase angle for the same geometrical parameters. The white circles denote solutions in which the reflected energy is both low yet the transmitted phase angle varies by more than a full 360° range. It should be noted that much larger phase shifts are possible if ones uses electrically thicker substrates. It is from those solutions, denoted by the white circles in Figure 5, that our library of allowable grating structures is formed.

As multiple solutions with similar AR and transmission properties can be found, we imposed two additional design

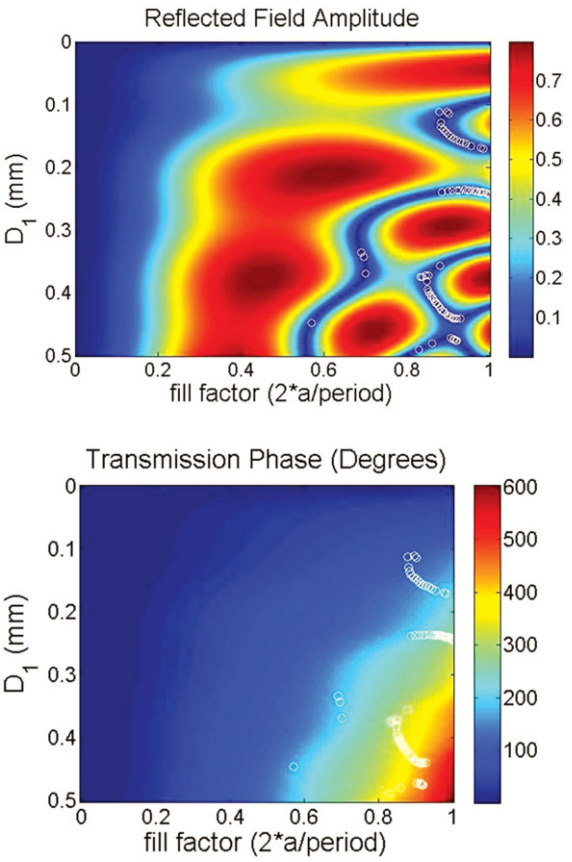

Figure 5 Calculated false color images of the reflected field amplitude (top image) and transmitted field phase (bottom image) as a function of fill factor ($2a/\Lambda$) and hole depth , d_1, of the geometry shown in Figure 2. For these calculation $\lambda = 1.0$, $d_o = 1.0$ and $n_{\text{substrate}} = 3.0$. The white circles denote points in which the reflected energy is low (<5%) yet the transmitted phase angle varies over a full 360° range. [Color figure can be viewed in the online issue, which is available at wileyonlinelibrary.com]

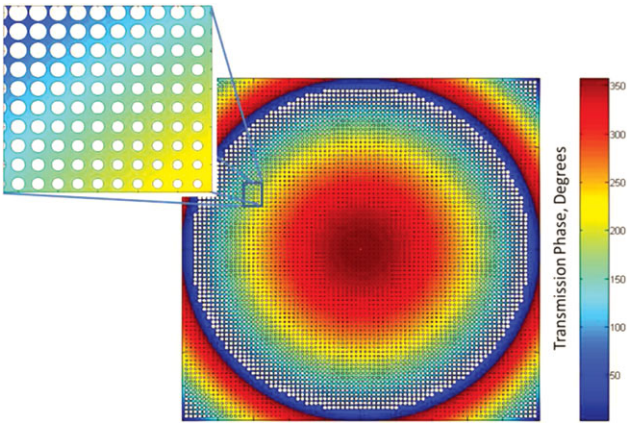

Figure 6 Illustration of mapping between desired phase and subwavelength cylindrical feature size. Both the diameter and depth of each hole is determined locally using the precalculated look-up-table that minimizes reflection losses while best matching transmission phase. [Color figure can be viewed in the online issue, which is available at wileyonlinelibrary.com]

constraints when creating the lookup table. The first was constraining the look-up table, when possible, to only those solutions (i.e., fill-factors and hole depths) that could easily be fabricated. In this way, we are able to integrate fabrication constraints directly into the design algorithm. The second was to seek solutions, when possible, in which the half-space reflection coefficient was also low. We did this to avoid solutions that are too dependent on destructive interference effects from multiple passes across the entire sample. As those solutions are likely to create errors when extending the results to aperiodic structures, such as lenses. The half-space reflection coefficient was easily calculated by assuming an infinite thickness, d_o, in Figure 2.

2.4. Design Algorithm for Aperiodic GRIN Lenses

To design aperiodic elements in which the desired output phase varies spatially in the transverse plane [i.e., $\phi_{desired}(x,y)$] a spatial encoding scheme was used. In this process, a desired continuous phase response was sampled on a uniform two-dimensional (2D) grid where the grid spacing is small compared to the material wavelength (e.g., $\Delta < \lambda/3$) . At each spatial grid point, the subwavelength cylindrical feature (e.g., hole diameter and depth) that best matches the local phase was selected from the precalculated look-up table described in the previous section. As the look-up table only includes those grating geometries that have good impedance match, we would expect the entire aperiodic structure will also have low reflected losses. This process is illustrated in Figure 6.

It should be noted that the RCW results are only strictly valid when analyzing infinitely periodic structures. For aperiodic applications, we have made the assumption that the RCW results from the infinitely periodic case can be applied locally with only small errors. This is a common method used by other authors [14–16] in creating aperiodic subwavelength diffractive elements. We have found through numerous examples that this works well as long as the phase variation does not change too abruptly compared to the wavelength.

3. NUMERICAL AND EXPERIMENTAL VALIDATION

To validate our method, we designed fabricated and characterized three samples. These were (1) four quadrant phase plate, (2) one dimensional GRIN lens (i.e., cylindrical lens), and (3) two dimensional GRIN lens (i.e., spherical phase lens).

3.1. Numerical Validation

The finite element method (FEM) was used to simulate the entire aperiodic flat lenses before, we proceeded to fabrication and testing. The FEM program used to simulate the test structures was ANSYS's high frequency structural simulator (HFSS). To simulate the electric far field propagation, the HFSS transmitted near field was applied to Rayleigh–Sommerfield integration equations.

3.2. Experimental Validation

To characterize the experimental samples, we used the setup depicted in Figure 7. At the heart of this setup is an Agilent PNA vector network analyzer (VNA) with external heads that extend the frequency range from 20 MHz to 110 GHz. On the transmit side a standard gain horn, placed in the far-field of the sample, was used to form a quasi-plane wave at the surface of a square entrance aperture $10'' \times 10''$ in size. The sample was surrounded with radar absorbing material (RAM) to minimize diffraction effects from the edge of the sample. On the receive side a small microwave detector, attached to a xyz translation system, was used to measure the transmitted magnitude and phase as a function of space. An external computer was used to control and coordinate the *xyz* translation and VNA measurements. The entire setup was constructed inside a larger chamber covered with RAM on all surfaces to minimize external interference. Frequency averaging and time-domain gating were also used to remove extraneous reflections.

3.3. Sample #1: Four Quadrant Phase Plate

The first sample that was designed, fabricated, and characterized was the simple four quadrant phase plate, shown in Figure 8. Each quadrant in Figure 8 was designed to have a different transmitted phase with near 100% transmitted magnitude at a center frequency of 26 GHz. The sample was fabricated from a $12'' \times 12'' \times 0.5''$ dielectric plate made from HiK material (Emerson & Cuming). We measured the dielectric constant of the plate to be $\varepsilon_{substrate} = 4.0$ with a negligible loss term. Based on the RCW simulations and additional design criteria discussed in the previous section, we selected the grating structures for the

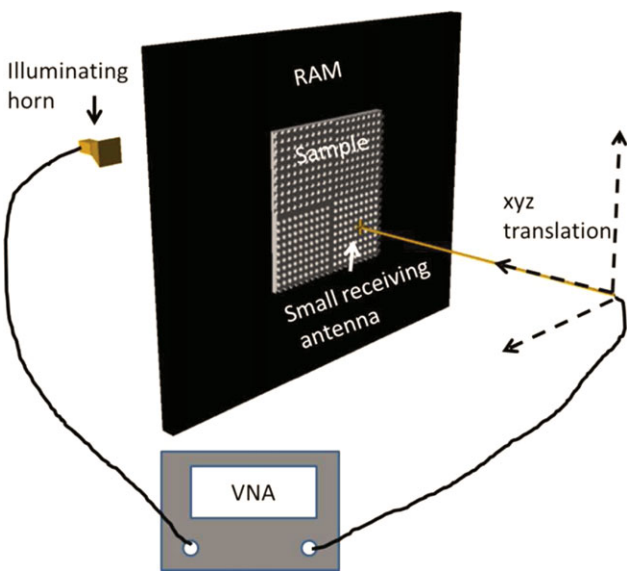

Figure 7 Illustration of the test setup used to experimentally characterize the fabricated samples. [Color figure can be viewed in the online issue, which is available at wileyonlinelibrary.com]

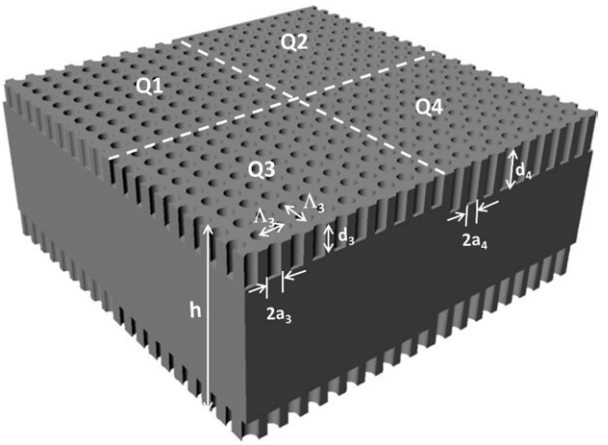

Figure 8 Illustration of sample #1—a four quadrant phase plate with integrated AR properties

four regions shown in Table 1. Using computer numerically controlled (CNC) milling, we fabricated the subwavelength structure shown in Figure 8.

After measuring the geometrical features of the fabricated sample and its transmission characteristics, using the system described in Figure 7, we obtained the results given in Table 2. Here, transmission measurements were taken in the center of each of the four quadrants. Because of slight fabrication errors, the measured surfaces had hole depths and radii slightly different from the designed values given in Table 1.

The predicted response, given in Table 2, is for the measured sample parameters. The measured transmission properties at 26 GHz match the predicted values reasonably well. The maximum %error is 8.5% in transmitted phase and 3% in transmitted amplitude. It should be noted that for all four quadrants the maximum transmission loss is only 4% with a mean value of 1.75%. For an identical dielectric slab, ($\varepsilon_{substrate} = 4.0$, $h = 12.7$ mm) without any AR surface treatment the transmission loss at 26 GHz would have been 17.5%.

3.4. Sample #2: Cylindrical Phase GRIN Lens

The second sample, we designed and tested was the cylindrical lens shown in Figure 9. Here, the sample was designed to have a parabolic phase profile with a maximum phase variation of 180° along the horizontal axis and constant phase along the vertical axis (depicted in Fig. 9). The substrate used to realize this sample was a 12.7-mm thick plate of HiK with a dielectric constant of $\varepsilon_{substrate} = 6.0$. The lens was designed to create a line focus at a focal distance of 300 mm for an incident frequency of 26 GHz. The aperture size of the lens was 120×120 mm^2 ($F\# = 2.5$). To realize this cylindrical lens with integrated AR properties, we used the design algorithm described previously. A periodicity of 2.3 mm (i.e., one-fifth the free-space wavelength) was used for the hole array.

TABLE 1 Design Parameters for Sample #1

	Q1	Q2	Q3	Q4
Hole depth, d (mm)	1.6	2.5	5.0	5.5
Hole radius, a (mm)	1.51	1.66	1.46	1.58
Slab thickness, h (mm)	12.7	12.7	12.7	12.7
Period, Λ (m)	3.0	3.0	3.0	3.0
Desired transmission phase (°)	−130	−60	10	50
Predicted transmission magnitude	0.998	0.976	0.999	0.999

TABLE 2 Measured Parameters for Sample #1

	Q1	Q2	Q3	Q4
Hole depth, d (mm)	1.7	2.6	5.1	5.5
Hole radius, a (mm)	1.51	1.68	1.47	1.58
Slab thickness, h (mm)	12.6	12.6	12.6	12.6
Period, Λ (mm)	3.0	3.0	3.0	3.0
Predicted transmission phase (°)	−112.4	−50.4	11.2	50.9
Predicted transmission magnitude	0.99	0.97	0.99	0.99
Measured transmission phase (°)	−116.0	−54.7	11.2	52.9
Measured transmission magnitude	0.99	0.96	0.99	0.99

A HFSS model was first used to simulate the response of the cylindrical lens. For this example a mirror symmetry plane was used to reduce the computation time. After numerical validation using HFSS the sample shown in Figure 9 was fabricated using CNC machining.

To measure the transmission properties of the sample, we used the experimental system described previously. A small monopole antenna was used as the detector and scanned along the line and plane shown in Figure 10(a) and 10(b), respectively. At each location, the magnitude and phase of the transmission coefficient was measured experimentally and calculated using HFSS.

Figure 11 compares the desired transmission characteristics against the HFSS simulated and experimentally measured results for the line scan depicted in Figure 10(a). The transmitted phase [Fig. 11(b)] shows a close match between the desired, simulated, and measured values. The magnitude of the transmission coefficient [Fig. 11(a)] varies considerably over the surface of the sample due to the aperiodic nature of the sample (i.e., internal refraction and diffraction); however, the average magnitude for the transmission coefficient across the sample is 0.97. As a comparison a homogenous plate of the same thickness and dielectric constant would have a transmission coefficient magnitude of 0.72 at 26 GHz. This is a clear indication that the sample was able to generate the proper phase distribution while simultaneously providing integrated AR properties.

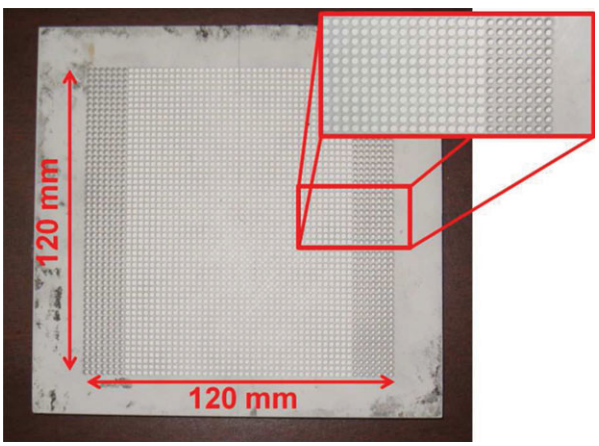

Figure 9 Sample #2 is a cylindrical lens fabricated from Emerson and Cumming HiK dielectric of $\varepsilon_r = 6.0$. [Color figure can be viewed in the online issue, which is available at wileyonlinelibrary.com]

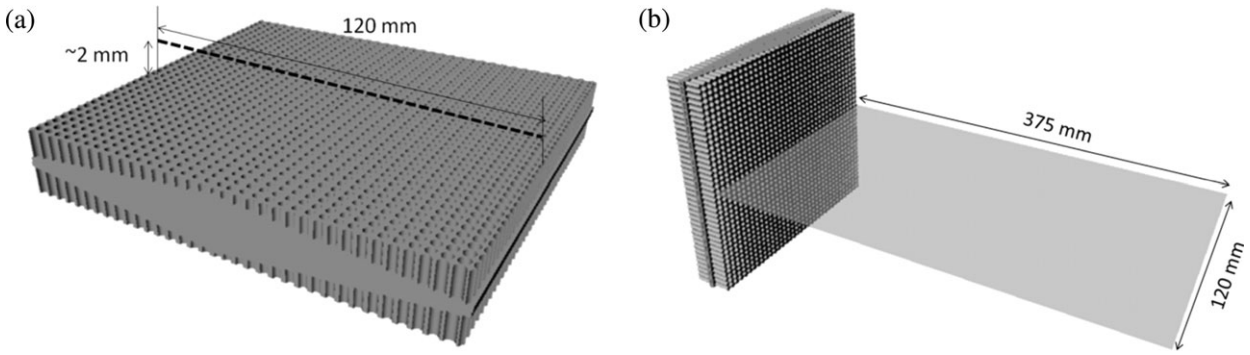

Figure 10 Illustration of the experimental scans used to measure the response of sample #2. (a) Line scan across the horizontal axis (Fig. 9). The detector was placed a very short distance from the surface of the sample (∼2 mm) and centered along the vertical axis (Fig. 9). (b) Scan in a 2D plane in s was selected to encompass the focal region of the lens

In Figure 12, we show the HFSS simulated and measured transmission coefficient magnitude within the plane depicted in 10(b). Here, the measured and simulated results compare well, with a very distinct focus obtained at the designed focal distance of 300 mm.

3.5. Sample #3: 2D Spherical Phase GRIN Lens

The last sample that was designed, fabricated, and characterized was the 2D spherical phase GRIN lens shown in Figure 13. Here, the sample was designed to have a spherical phase profile with a maximum phase variation of 345°. As in sample #2, we used a 12.7-mm thick plate of HiK ($\varepsilon_{substrate} = 6.0$) to fabricate the lens. The lens was designed to create a point focus at a focal distance of 220 mm at an incident frequency of 26 GHz. To realize this spherical lens with integrated AR properties, we employed the design algorithm described previously. As in the previous example, a periodicity of 2.3 mm (i.e., one-fifth the free-space wavelength) was used for the hole array.

In Figure 14, we compare the designed, HFSS simulated, and experimentally measured results for the line scan depicted in

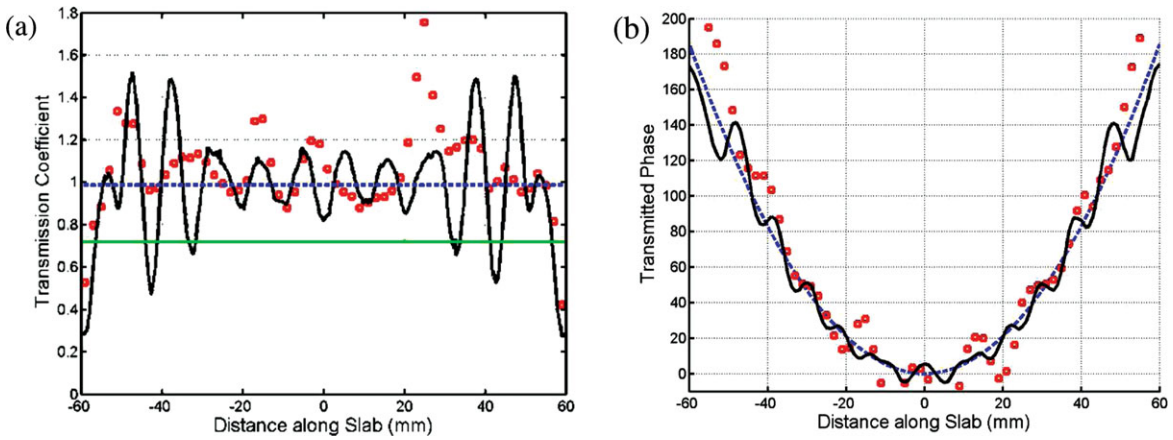

Figure 11 Magnitude [11(a)] and phase [11(b)] of the transmission coefficient for the cylindrical lens at 26 GHz. Data was collected along the surface of the lens [shown in Fig. 10(a)] Here, experimental data (-□-), desired magnitude (----), 12.7 mm dielectric slab of $\varepsilon_r = 6$ (——), and HFSS near field (——) for the spherical flat lens. [Color figure can be viewed in the online issue, which is available at wileyonlinelibrary.com]

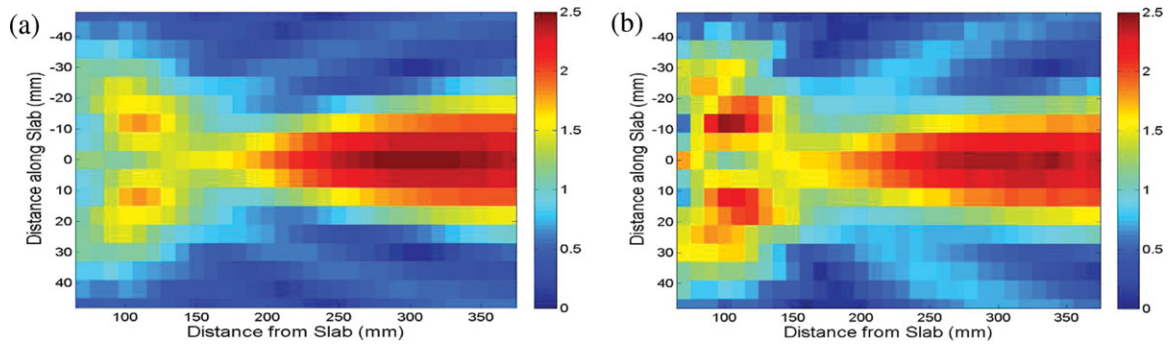

Figure 12 Magnitude of the transmission coefficient for the cylindrical lens shown in Figure 9 in the plane depicted in Figure 10(b). (a) HFSS simulated results and (b) experimentally measured results. [Color figure can be viewed in the online issue, which is available at wileyonlinelibrary.com]

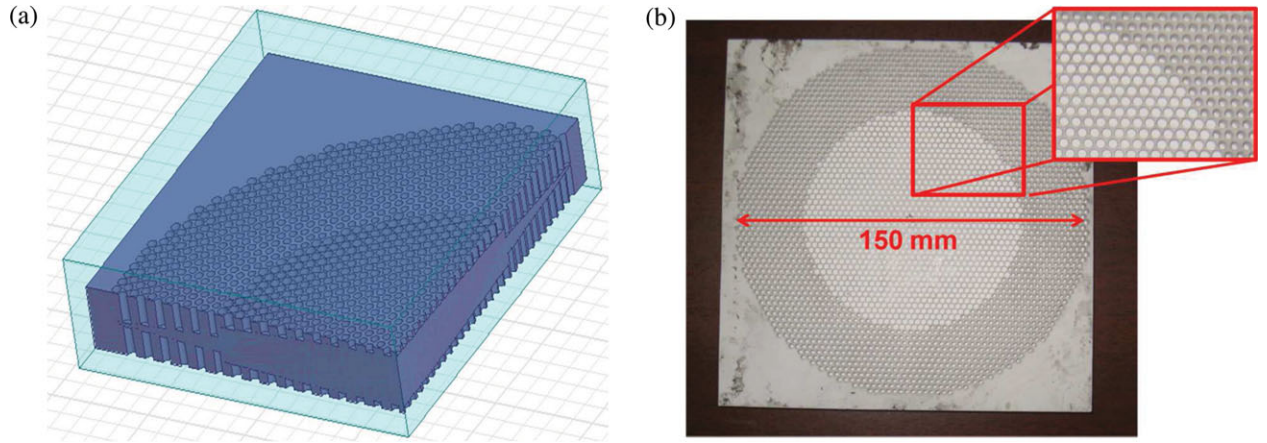

Figure 13 Sample #3 is a 2D spherical phase lens (a) HFSS model and (b) fabricated lens. [Color figure can be viewed in the online issue, which is available at wileyonlinelibrary.com]

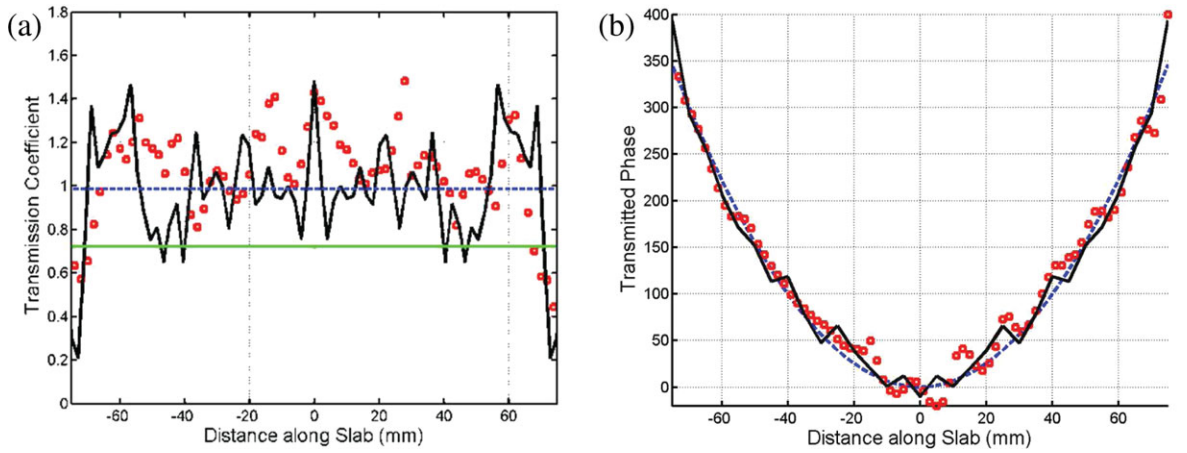

Figure 14 Magnitude (a) and phase (b) of the transmission coefficient for the spherical phase GRIN lens at 26 GHz. Data was collected along the surface of the lens [shown in Figure 10(a)] Here, experimental data (-□-), desired magnitude (----), 12.7 mm dielectric slab of $\varepsilon_r = 6$ (——), and HFSS near field (——) for the spherical flat lens. [Color figure can be viewed in the online issue, which is available at wileyonlinelibrary.com]

Figure 10(a) at an incident frequency of 26 GHz. As in the previous example, the spherical phase lens shows good agreement between the design, HFSS simulation, and experimental results. The average magnitude of the transmission coefficient [Fig. 14(a)] for this sample was 0.98 compared to 0.72 for the homogenous plate of the same thickness and dielectric constant.

In Figure 15, we show the HFSS simulated and measured transmission coefficient magnitude within the plane depicted in

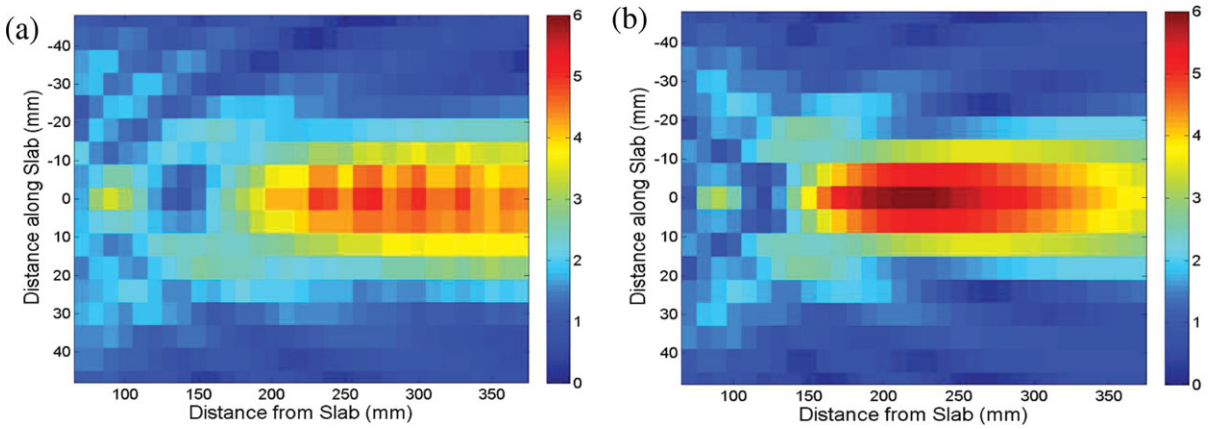

Figure 15 Magnitude of the transmission coefficient for the spherical phase GRIN lens shown in Figure 13 in the plane depicted in Figure 10(b). (a) experimentally measured results and (b) HFSS simulated results. [Color figure can be viewed in the online issue, which is available at wileyonlinelibrary.com]

TABLE 3 Summary of Transmission Results from the Three Test Samples Presented at 26 GHz

		Ave. $\lvert T\rvert$	Ave. $\angle T°$ error
Homogenous dielectric slab ($\varepsilon_r = 6.0$, $h = 12.7$ mm)	Design	0.72	NA
	HFSS	NA	NA
	Measured	NA	NA
Sample #1: Four quadrant phase plate	Design	0.99	NA
	HFSS	0.98	NA
	Measured	0.98	5.9
Sample #2: Cylindrical GRIN lens	Design	0.99	NA
	HFSS	0.98	1.4
	Measured	0.97	11.5
Sample #3: Spherical phase GRIN lens	Design	0.98	NA
	HFSS	0.97	12.7
	Measured	0.98	12.8

What is presented is the average magnitude and the average phase error of the transmission coefficient.

Figure 10(b). Here, the measured and simulated results again compare well, with a very distinct focal spot obtained at the designed focal distance of 220 mm.

3.6. Summary of Results

In Table 3, we summarize the designed, simulated and experiment results from the three samples. Presented are the average measured transmission coefficient magnitude (averaged over the surface of the sample) and the maximum phase error between predicted results (i.e., HFSS) and measured results. Also provided in the table is the predicted transmission magnitude of a homogenous dielectric slab of the same thickness and dielectric constant as the substrates used to fabricate the samples. It is clear from Table 3 that each of the samples did indeed provide improved AR properties, compared to the homogenous slab, while achieving the desired transmitted phase distributions.

4. CONCLUSIONS

A method was presented for developing a GRIN flat lens with integrated AR properties. The method was based on the use of subwavelength grating structures that can be designed to have low reflected losses for a wide range of transmitted phases. Several samples were designed, fabricated, and characterized to validate our design methodology. One advantage of this approach is the ability to significantly shrink the thickness of the element by using higher dielectric constant substrates while simultaneously minimizing reflected losses. Future work will focus on expanding the method to achieve higher operational bandwidths.

ACKNOWLEDGMENT

This work was sponsored by ONR 331.

REFERENCES

1. D.W. Prather, J.N. Mait, M.S. Mirotznik, and J.P. Collins, Vector-based synthesis of finite aperiodic subwavelength diffractive optical elements, J Opt Soc Am A 15 (1998), 1599–1607.
2. M.S. Mirotznik, T. Creazzo, and S. Matthews, Design of diffractive elements at millimeter wavelengths using subwavelength cylindrical microstructures, Microwave Opt Technol Lett 49 (2007), 1880–1884.
3. U. Levy, M. Nezhad, H. Kim, C. Tsai, L. Pang, and Y. Fainman, Implementation of a graded-index medium by use of subwavelength structures with graded fill factor, J Opt Soc Am A 15 (2005), 724–732.
4. Z.L. Mei, J. Bai, and T.J. Cui, Gradient index metamaterials realized by drilling hole arrays, J Phys D Appl Phys (2010).
5. J.M. Nowosielski, R. Buczynski, F. Hudelist, A. Waddie, D. Pysz, R. Stepien, I. Kujawa, and M.R. Taghizadeh, Focusing gaussian beam in nanostructured non-periodic GRIN microlenses, Phonton Lett Pol 2 (2010), 34–36.
6. M.S. Mirotznik, B.L. Good, P. Ransom, D. Wikner, and J.N. Mait, Iterative design of moth-eye antireflective surfaces at millimeter wave frequencies, Microwave Opt Technol Lett 53 (2010).
7. M.S. Mirotznik, B. Good, P. Ransom, D. Wikner, and J.N. Mait, Design of inverse moth-eye antireflective surfaces, IEEE Trans Antennas Propag 58 (2010), 2969–2980.
8. J. Santos and L. Bernado, Antireflective structures with use of multilevel subwavelength zero-order gratings, Appl Opt 36 (1997), 8935–8938.
9. R. Brauer and O. Bryngdahl, Design of antireflective gratings with approximate and rigorous methods, Appl Opt 33 (1994), 7875–7882.
10. E. Noponen and J. Turunen, Eigenmode method for electromagnetic synthesis of diffractive elements with three-dimensional profiles, J Opt Soc Am A 11 (1994), 2494–2502.
11. M.G. Moharam, D.A. Pommet, E.B. Grann, and T.K. Gaylord, Stable implementation of the rigorous coupled-wave analysis for surface-relief gratings: Enhanced transmittance matrix approach, J Opt Soc Am A 12 (1995), 1077–1084.
12. P. Lalanne, Improved formulation of the coupled-wave method for two-dimensional gratings, J Opt Soc Am A 14 (1997), 1592–1598.
13. F. Languy, K. Fleury, C. Lenaerts, J. Loicq, D. Regaert, T. Thibert, and S. Habraken, Flat Fresnel doublets made of PMMA and PC: Combining low cost production and very high concentration ratio for CPV, Opt Expr 19 (2011).
14. B.H. Kleemann, M. Seeßelberg, and J. Ruoff, Design concepts for broadband high-efficiency EA-DOEs, DGaO Proceedings, 2008.
15. S. Takahashi, C. Chang, S.Y. Yang, and G. Barbastathis, Design and fabrication of dielectric nanostructured Luneburg lens in optical frequencies, In: Optical MEMS and Nanophotonics (OPT MEMS) International Conference, 2010.
16. P. Lalanne and D. Lemercier-lalanne, On the effective medium theory of subwavelength periodic structures, J Mod Opt 43 (1996).

DUAL-BAND/DUAL-POLARIZED MICROSTRIP PATCH ANTENNA FOR DUAL-BAND HETERODYNE RETRODIRECTIVE ARRAY

Dong-Jin Jung, Jonathan N. Hansen, and Kai Chang
Department of Electrical and Computer Engineering Texas A&M University College Station, TX 77843-3128; Corresponding author: dongjin3558@tamu.edu

Received 24 March 2012

ABSTRACT: *This article presents a dual-band/dual-polarized microstrip patch antenna. For a dual-band retrodirective array system, the dual-band/dual-polarized microstrip patch antenna operating at 11 and 12.2 GHz is designed and tested. The antenna consists of one rectangular microstrip patch and a square ring outside of the patch. Two different feeding locations are used for vertical and horizontal polarizations. The vertical polarization is used for a receiving mode and the horizontal polarization for a transmitting mode. The antenna shows a measured gain of 5.2 and 6.8 dBi at 10.9 and 12.2 GHz. The isolation*